Towards integrated fiber-optic distributed acoustic and magnetic sensing: Theory, simulation, and observation

Tomas Snyder[1], Shihao Yuan[1], Eileen R. Martin[1],

Daniel Homa[2], Zach Dejneka[2], Gary Pickrell[2], Anbo Wang[3], Logan Theis[3]

[1] *Center for Wave Phenomena, Colorado School of Mines, Golden, CO 80401*
[2] *Center for Photonics Technology, Virginia Tech, Blacksburg, VA 24061*
[3] *Sentek Instrument, LLC, Blacksburg, VA 24060*
email: tsnyder1@mines.edu

ABSTRACT

Breakthroughs in distributed optical fiber sensing have enabled continuous recording of seismic data (strain/strain rate), resulting in unparalleled spatial resolution and coverage at a more affordable cost in hard-to-reach areas. However, distributed electromagnetic sensing systems are still in the prototype stage. This study explores a novel multi-physics optic fiber that records seismic and magnetic wavefields simultaneously. The magnetostrictive effect formulates the basic measuring principle of the proposed distributed magnetic sensing. Field experiments using a solenoid and bass shaker are conducted to test sensitivity to both magnetic and acoustic signals. The magnetic spectral response observed in the field is consistent with that predicted by the theoretical model. The preliminary field results and cross-well controlled source electromagnetic simulations demonstrate the potential of the proposed multi-physics fiber optic sensing system for monitoring fluid injection and pave the way for further research and development of an integrated distributed acoustic and magnetic sensing system.

Key words: Distributed fiber optic sensing, Controlled source electromagnetic, Geophysical imaging and monitoring, CO_2 sequestration

1 INTRODUCTION

Distributed magnetic sensing is a technology that combines the existing capability of distributed acoustic sensing with novel fiber cables that respond to magnetic fields. In particular, this is done through coupling a fiber optic to a material that expands or contracts in response to magnetic fields, known as a magnetostrictive material. In this way, as the magnetostrictive material responds, it also imparts a force on the fiber optic cable, and that strain on the cable can then be measured by a laser using the distributed acoustic sensing measurement principles. The fiber optic magnetic sensing design that we focus on in this report is described along with initial laboratory tests in Hileman et al. (2022). A diagram of this design with embedded magnetostrictive rods inside the fiber optic is shown in Figure 1. In addition to responding to magnetostriction-induced strain, the measurements also respond to other sources of strain (e.g. temperature-related expansion or contraction and mechanical strains), so quantitative modelling of these new fiber optic material responses is critical to data analysis and interpretation.

This report outlines the preliminary efforts to quantitatively model this novel fiber optic magnetic sensing system. To understand this, we take a two-pronged approach: (i) understand the small-scale response of the magnetostrictive materials, and (ii) understand the field-scale needs and expected response of the system. We start with the basic theory of magnetostriction and provide a brief theoretical review of how electromagnetic geophysical methods work. Based on these theoretical models, we provide small-scale computational modelling of the range of responses to controlled magnetic fields, then provide computational modelling of the expected responses to a cross-well experimental setup. We describe the design of our first small-scale near-surface field trial, and provide preliminary analysis of the data from this first field trial, which is now being used to make further improvements in both the sensitivity of the proposed sensing system to multiple parameters, and the design of field experiments.
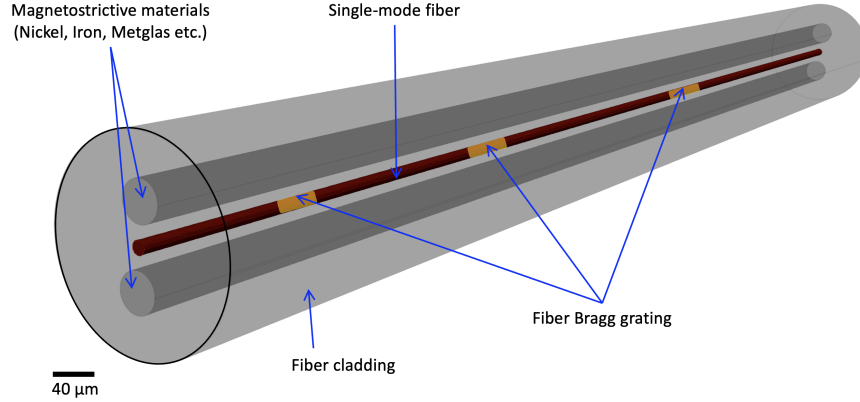
Figure 1. Schematic illustration of the distributed acoustic and magnetic sensing fiber

2   THEORY AND BACKGROUND

2.1   Magnetostriction Modeling Theory

Magnetostriction is the strain induced in a ferromagnetic material (e.g. Iron, Nickel, and Cobalt) by an external magnetic field, $\vec{H}$. Ferromagnetic materials exhibit variable and relatively large magnetic permeability, χ, relatively large magnetic saturation values M_s, and hysteresis in their magnetic response. These properties are attributable to domains of magnetization, within the material containing many atoms with magnetic dipoles oriented in the same direction, as shown in Figure 2. Domains are a quantum mechanical phenomenon which have magnetization magnitudes at the saturation value (Cullity and Graham, 2009). When a ferromagnetic material is in an ideal demagnetized state (i.e. all magnetic domain orientations are of the same volume), the material exhibits a zero net external magnetic field. When $\vec{H}$ is applied to the material, the domain magnetic moments $\vec{M}$ experience a torque per volume, $\vec{N} = \vec{M} \times \vec{H}$, which aligns the overall magnetic moment of the material in the direction of $\vec{H}$ if $||\vec{H}||$ is large enough to saturate the material, thus magnetizing the material even after $\vec{H}$ is turned to zero. The Landau-Lifshitz-Gilbert (LLG) equation,

$$\frac{d\vec{M}}{dt} = \gamma(\vec{M} \times \vec{H}) - \frac{\alpha}{M}\left(\vec{M} \times \frac{d\vec{M}}{dt}\right) + \gamma\alpha^2(\vec{M} \times \vec{H}), \tag{1}$$

describes the motion of the total magnetic moment of a ferromagnetic material (Gilbert, 2004; Wieser, 2015), accounting for damping of the domain motion. In eqn. 1, the constant $\gamma = ge/2mc$, where e and m are the charge and mass of the electron, c is the speed of light, and g is the spectroscopic splitting factor ($g = 2$ for electron spin); and the damping term $\alpha = \lambda/\gamma M$, where λ is an adjustable damping parameter.

If the cubic structure of the material is not exactly cubic (e.g. tetragonal or rhombohedral) the material undergoes a change in length Δl, and a subsequent strain $\Delta l/l$, when the domains are reoriented. The strain experienced by an anisotropic cubic crystal when magnetized from the ideal demagnetized state to saturation in the direction defined by the direction cosines α_1, α_2, and α_3 and measured in the direction defined by the direction cosines β_1,β_2, and β_3 relative to the crystal axes is

$$\lambda_{si} = \frac{3}{2}\lambda_{100}\left(\alpha_1^2\beta_1^2 + \alpha_2^2\beta_2^2 + \alpha_3^2\beta_3^2 - \frac{1}{3}\right) + 3\lambda_{111}(\alpha_1\alpha_2\beta_1\beta_2 + \alpha_2\alpha_3\beta_2\beta_3 + \alpha_3\alpha_1\beta_3\beta_1), \tag{2}$$

where λ_{100} and λ_{111} are the saturation magnetostrictions in the [100] and [111] crystal directions (Cullity and Graham, 2009). Assuming the magnetostriction of the material is isotropic simplifies eqn. 2 to

$$\lambda_\theta = \frac{3}{2}\lambda_s\left(\cos^2\theta - \frac{1}{3}\right), \tag{3}$$

where λ_s is the isotropic saturation magnetostriction and θ is the angle between the measurement direction and the saturated direction. While magnetostriction is typically not isotropic in materials, approximating the response as isotropic works well for materials with anisotropic magnetostrictions close in value, like Nickel which has saturation magnetostriction values $\lambda_{100} = -46\ ppm$, $\lambda_{111} = -24\ ppm$, and $\lambda_s = -34\ ppm$ (Hileman et al., 2022) - the negative sign indicates a decrease in length.
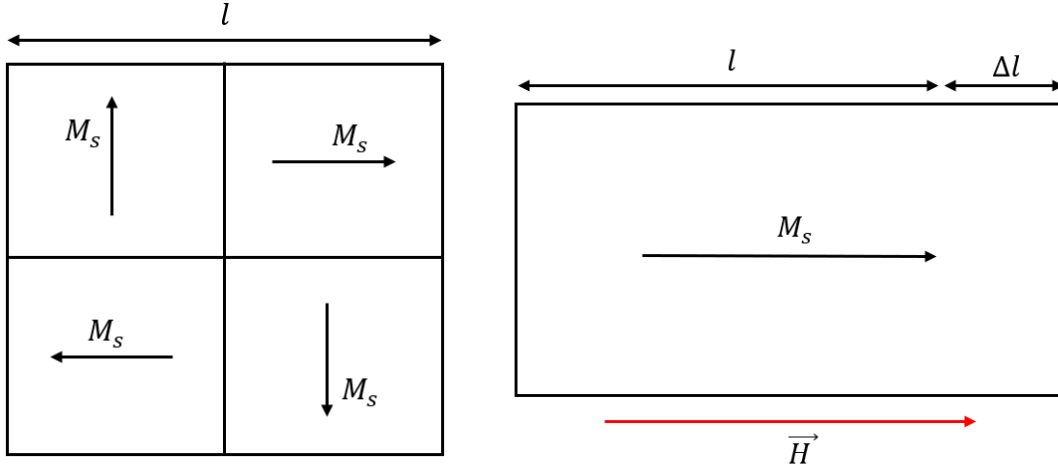
Figure 2. The domains within a ferromagnetic material are sections of magnetic saturation M_s, with magnetization vectors oriented in different directions. The net magnetic field outside the material due to the internal magnetic moments is zero when not magnetized by an external magnetic field (left). When a magnetic field $\vec{H}$ is applied to the material, the magnetic dipoles align in the direction of the external field, causing a change in length Δl (right).
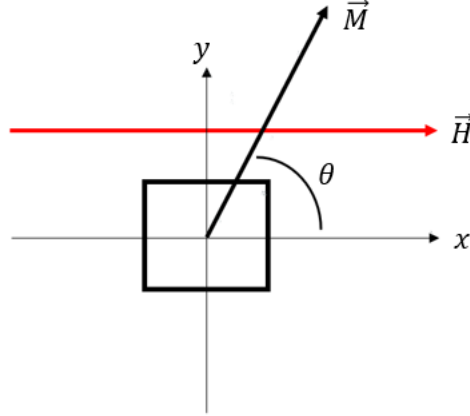

Figure 3. A visualization of the model setup. The x direction is also the strain measurement direction, with saturation occurring in the direction of $\vec{M}$, where $||\vec{M}|| = M_s$.

3   COMPUTATIONAL MODELLING

3.1   Two-dimensional magnetostriction modelling

The model of magnetostriction assumes a piece of material in two-dimensions with a single domain that is magnetostrictively isotropic and homogenenous. The external magnetic field is a uni-directional, spatially uniform, alternating sinusoidal magnetic field, which is in the same direction as the strain measurement , Figure 3. These assumptions simplify eqn. 1 to

$$\frac{d\theta}{dt} = -\gamma \frac{1 + \alpha^2}{1 + \alpha} H_0 \sin(\omega t - \phi) \sin\theta. \tag{4}$$

Here, θ is defined the same as in eqn. 3 such that the two equations can be combined to solve for magnetostriction along a single axis. The other variables are the magnetic field amplitude of the source H_0, source angular frequency ω, and phase of the source ϕ. To solve eqn. 4, the Dormand-Prince method of solving ordinary differential equations (Dormand and Prince, 1980) is implemented with ode45 in MATLAB. The resulting θ is then substituted into eqn. 3 to solve for the strain response. A similar approach to solving for the dynamic magnetostriction response was used in Shoemaker (2018), with a different method to solve for θ, that was
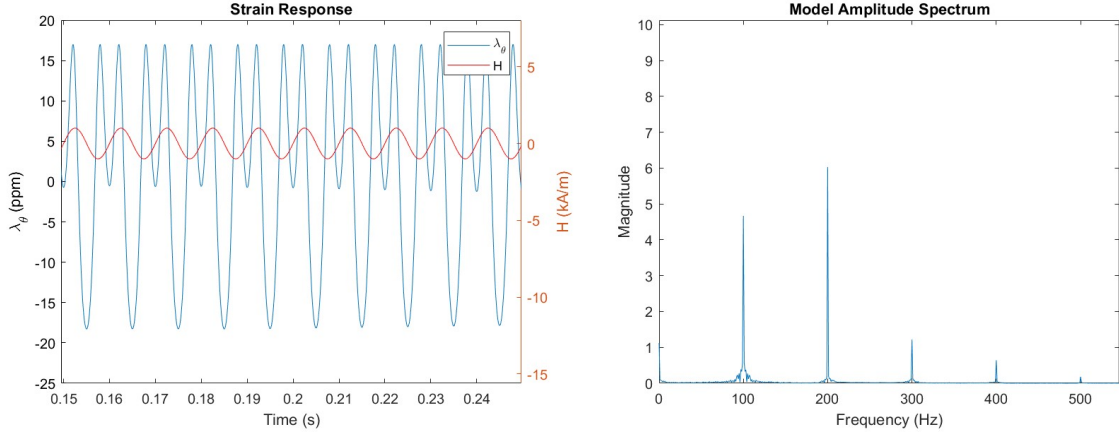
Figure 4. Example outputs of the strain response (left) and model amplitude spectrum (right) for a 100 Hz source with a source amplitude of $H_0 = 1\, kA/m$.

successful at predicting frequency doubling but not the harmonics. An example of the strain response of Nickel to a 100 Hz source with amplitude 1 kA/m and a phase of zero is shown in Figure 4. The amplitude spectrum of the magnetostrictive response reveals strain oscillations occurring at the source frequency, double the source frequency, and at harmonics of the source frequency. The source frequency and double frequency responses are due to large angular motions of the domain while the harmonics are due to small scale angular oscillations of the domain.

The amplitudes of the signals in the amplitude spectrum are highly sensitive to changes in H_0, the initial angle of $\vec{M}$ with $\vec{H}$, θ_0, and the source frequency f_s. The response frequencies also have significant dependence on f_s. To demonstrate the dependence of the response amplitudes on H_0, a suite of simulations showing the response amplitudes for different values of H_0 at $f_s = 100$ Hz and $\theta_0 = \pi/3$ is shown in Figure 5. At values of H_0 below 8 kA/m, the response amplitudes follow fairly steady trends, with the harmonics increasing in amplitude as the response at the driving frequency decreases. Between 8 kA/m and 10 kA/m, all the response amplitudes decrease by about an order of magnitude. Between 10 kA/m and about 18 kA/m, the response amplitudes increase again but evolve in a different manner - it is difficult to determine any trend in this region. After 18 kA/m, the even harmonics dominate the signal while the odd harmonics have some spikes in amplitude at certain values of H_0, possibly at predictable intervals. Since the response is largest and fairly predictable on the interval 1 $kA/m < H_0 < 8\, kA/m$, this may be a favorable external magnetic field amplitude to take measurements at.

The nonlinear nature of the LLG equation causes the observed sensitivity to the source amplitude (Taylor, 2005). In addition, nonlinear equations can exhibit high sensitivity to initial conditions (Taylor, 2005), θ_0 in this model. To demonstrate this sensitivity, the difference between the trajectories of θ over time between two different initial conditions $\theta_0^1 = 2\pi/3$ and $\theta_0^2 = 2\pi/3.01$ for $f_s = 100$ Hz and $H_0 = 10\, kA/m$ is shown in Figure 6. The trajectory of the magnetic dipole moments are similar initially, however, after about 7.5s they begin to diverge. This also results in difference in the strain response and amplitude spectra of the two simulations. This is a typical trait of nonlinear systems (Taylor, 2005), suggesting that the system we are studying may be chaotic under certain conditions (more research into this needs to be performed to determine whether or not this system exhibits chaos). Some studies have shown this chaos effect from the LLG equation under certain conditions (Lakshmanan (2011) and Smith et al. (2010)). It will be important to understand this response to interpret data from the fiber when it is deployed for real measurements. Since the response is more similar for different initial conditions within the first few seconds, it might be useful to take advantage of this time frame and record measurements for five or fewer seconds (for a 100 Hz source).

The model exhibits an expected response frequency dependence on f_s and, interestingly, dependence of the response *magnitude* on f_s. Two amplitude spectra for different source frequencies, $f_1 = 100$ Hz and $f_2 = 30$ Hz, at $H_0 = 1\, kA/m$ and $\theta_0 = 2\pi/3$ are shown in Figure 7. The response frequency dependence is apparent with responses to f_1 and f_2 at 100 Hz and 30 Hz, respectively, and harmonics at integer multiples of the source frequencies. There is an obvious difference in the amplitude of the fundamental frequency responses (100 Hz and 30 Hz) and the first harmonics (double-frequency, 200 Hz and 60 Hz) responses with the ratios of 0.06 and 1.3, respectively. There are also differences in the harmonic amplitudes between f_1 and f_2 in addition to the amount of harmonics present - the response to f_2 shows five more harmonics than f_1. In Figure 7, it shows that the amount of harmonics present may be also related to the ratio f_s/H_0. In the right panel of Figure 7, each source has a ratio of $f_s/H_0 = 10$ and we observe a more similar response between the two different sources than in the case when the ratios are different. Both responses
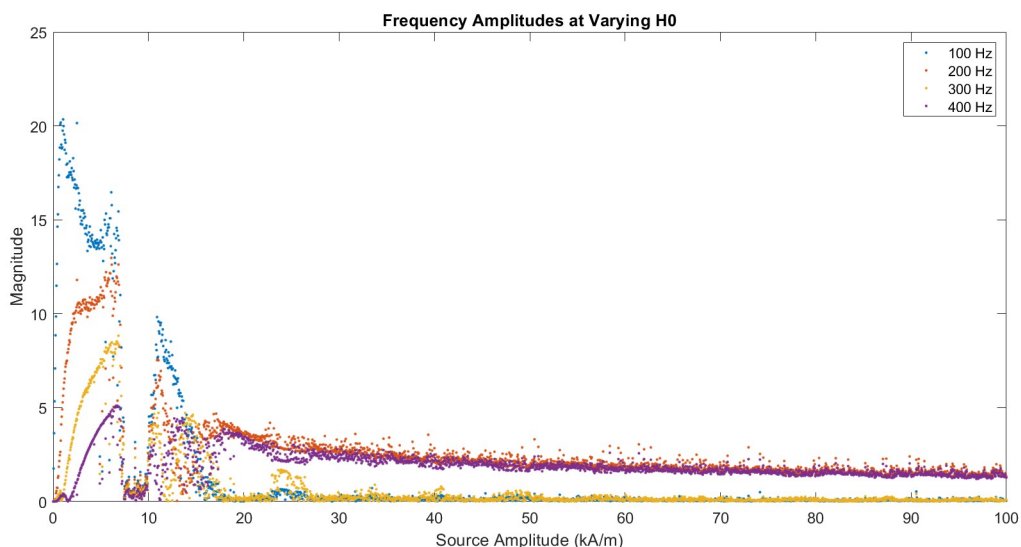
Figure 5. The variation of the response amplitudes at 100 Hz, 200 Hz, 300 Hz, and 400 Hz to a source with $f_s = 100$ Hz and magnetic field amplitude H_0. All frequencies e xamined have peak amplitudes below $8\,kA/m$ with a sudden drop in amplitude between $8\,kA/m$ and $10\,kA/m$. All signals then increase at $10\,kA/m$ then the even integer frequencies dominate the signal for increasing H_0.
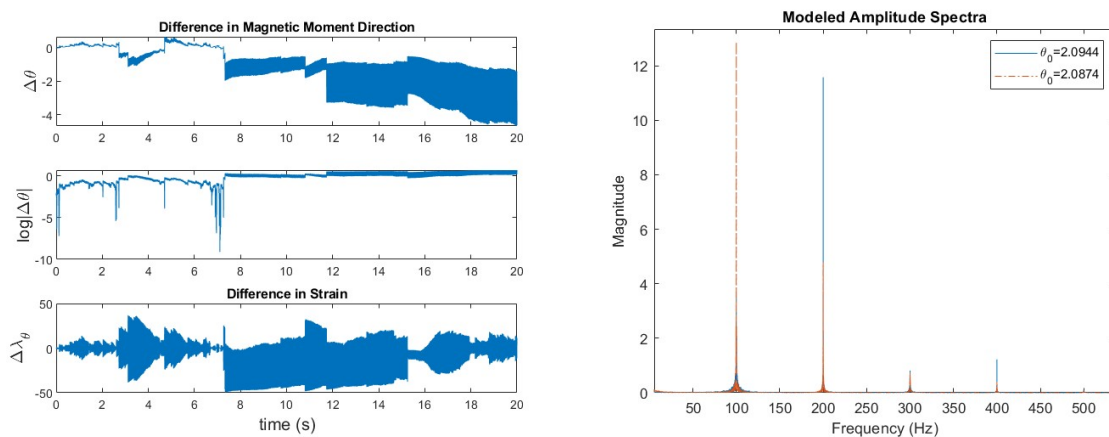

Figure 6. The difference in the response of two different initial conditions $\theta_0^1 = 2\pi/3$ and $\theta_0^2 = 2\pi/3.01$. (left) The difference of the magnetic moment direction over time for two simulations with the different initial conditions mentioned $\Delta\theta$, the log of the difference $\log|\Delta\theta|$ to show small scale variation, and the difference between the strain responses $\Delta\lambda_\theta$. (right) The amplitude spectra of both strain responses plotted on top of each other.

have the same number of significant response peaks; however, there are some small amplitude harmonics in the response to f_2 at 150 Hz and 180 Hz (≈ 0.08 amplitude) that are not visible in the response to f_1. In addition, the relative amplitudes of the response frequencies are different, but much closer in magnitude than the first simulation where f_s/H_0 is different. The double frequency responses are much closer than the source frequency responses, suggesting the double frequency response may be less sensitive to changes in f_s/H_0 than the source frequency response. While this modeling begins to show some of the features observed in the lab and field, further analysis is needed to carry out quantitative predictive modeling of the data we expect to record in any controlled-source experiment. Such predictive modeling is an essential element of any imaging or inversion procedure.
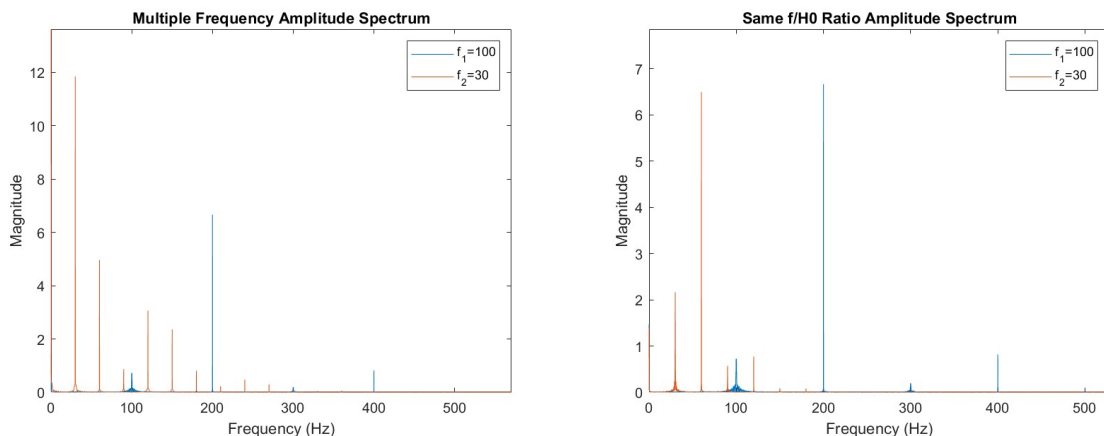
Figure 7. Amplitude spectra for two different source frequencies, f_1 and f_2. (left) The responses with the same H_0 for each source frequency. There is a clear difference in the amplitude of the source frequency response, double frequency response, and harmonics. (right) The responses with the same ratio f_s/H_0. The f_1 and f_2 response are more similar with the same amount of significant harmonics.

3.2   Cross-well controlled source electromagnetic simulation of CO_2 injection

The use of a cross-well controlled source electromagnetic (CSEM) survey can be advantageous in monitoring CO_2 injection because it can detect changes in electrical resistivity that occur when saline water is replaced by CO_2. To achieve two main objectives, a series of cross-well CSEM simulations were conducted with proposed magnetic optic fiber sensing system. The first objective was to establish a fundamental understanding of the sensitivity required for the magnetic optic fibers to detect and quantify electrical resistivity changes resulting from CO_2 injection. The second objective was to explore the potential benefits of using fiber optic cables instead of conventional EM sensors, which could lead to better spatial coverage during borehole CSEM surveys due to the ease of deployment. There are certain assumptions underlying the modeling, namely: (i) that the magnetic optic sensing fiber is well calibrated and that the magnetostrictive strain can be accurately converted to magnetic flux density, and (ii) that the acoustic strain and magnetostrictive strain can be separated. Based on these two assumptions, we were able to solve Maxwell's equations and analyze pure electromagnetic wave phenomena, without needing to consider a coupled magneto-mechanical system.

The time-lapse CSEM simulation is conducted using custEM, an open-source toolbox for 3D finite-element modeling of controlled-source, transient, and natural-source electromagnetic data (Rochlitz et al., 2019). Baseline modeling is performed using a cross-well configuration. The model consists of three layers and has dimensions of 500 m by 500 m by 1250 m in the X, Y, and Z directions (Figure 8). The baseline electrical resistivity of the layers is 100 $\Omega \cdot m$, 5 $\Omega \cdot m$, and 10 $\Omega \cdot m$, respectively. The time-lapse anomaly is a cubic shape measuring 80 m by 60 m by 20 m and is located at the center of the model at a depth of 400 m. The electrical perturbation resulting from CO_2 injection is assumed to be 10 times more resistive than the baseline model. This simple model aims to mimic CO_2 injection into a single sandstone layer saturated with saline water.

The transmitter well is located at an offset of 100 m from the central point of the time-lapse anomaly and is equipped with a vertical magnetic dipole source (VMD) at a depth of 400 m. The equivalent magnetic moment of the source is 3000 $A \cdot m^2$, transmitting electromagnetic waves of monofrequency. There are two horizontal wells in the X and Y directions, each with a vertical offset of 50 m, and one vertical well with a horizontal offset of 100 m. Each well contains a magnetic optic fiber measuring 100 m in length, with a channel spacing of 1 m.

In the first experiment, we employed a VMD source operating at a frequency of 100 Hz. Figure 9 shows the absolute amplitude difference between the time-lapse magnetic flux density recorded during the monitor and baseline surveys. Since the proposed distributed magnetic sensing method is sensitive only to magnetic fields along the fiber, we denote the magnetic flux density recorded along the optic fibers in three different receiver wells as Bx, By, and Bz, respectively. The results demonstrate that a sensitivity of approximately 0.1 nanotesla is required to detect the time-lapse magnetic response arising from CO_2 injection.

In the second experiment, we compare the relative time-lapse changes in magnetic response due to different resistivity perturbations. The two added time-lapse anomalies had the same dimension and resistivity but different dipping angles: one was horizontal and the other had a dipping angle of 60 degrees. We calculate the relative amplitude difference (δA) using the following equation:

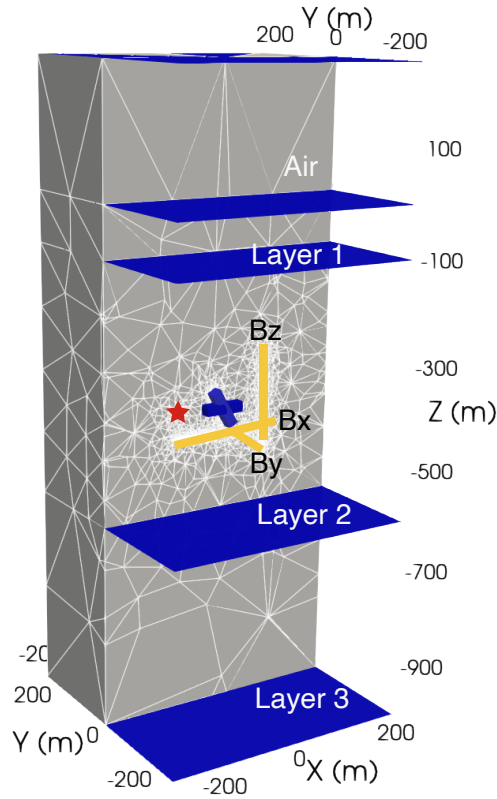$$\delta A = \frac{B^{mon} - B^{bas}}{B^{bas}} \times 100\%, \tag{5}$$

Figure 8. Geometry of the cross-well CSEM survey and time-lapse three-layer model of CO_2 injection. The red star denotes the vertical magnetic dipole source (VMD) and the three yellow lines denote three magnetic optic fibers. The two blue cubes represent one horizontal and one dipping resistive anomalies due to CO_2 injection.
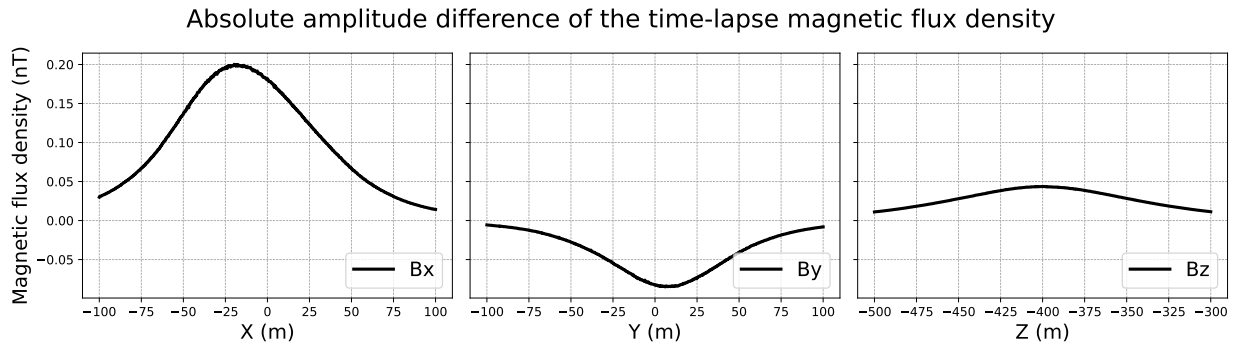

Figure 9. Absolute amplitude difference of the time-lapse magnetic flux density along the three magnetic sensing fibers shown in Figure 8. The time-lapse variations are caused by a horizontal resistive anomaly.

where B^{mon} and B^{bas} denote the magnetic flux density during monitor and baseline surveys, respectively. As shown in Figure 10, the maximum relative amplitude variations of the By component increase for the dipping resistivity anomaly compared to the horizontal anomaly, while the Bx and Bz components decrease. This suggests that the magnetic optic fibers, which can potentially provide more complete spatial coverage at a lower cost, making it possible to better detect and quantify CO_2-related electrical resistivity changes.

Relative amplitude changes of different resistive anomalies
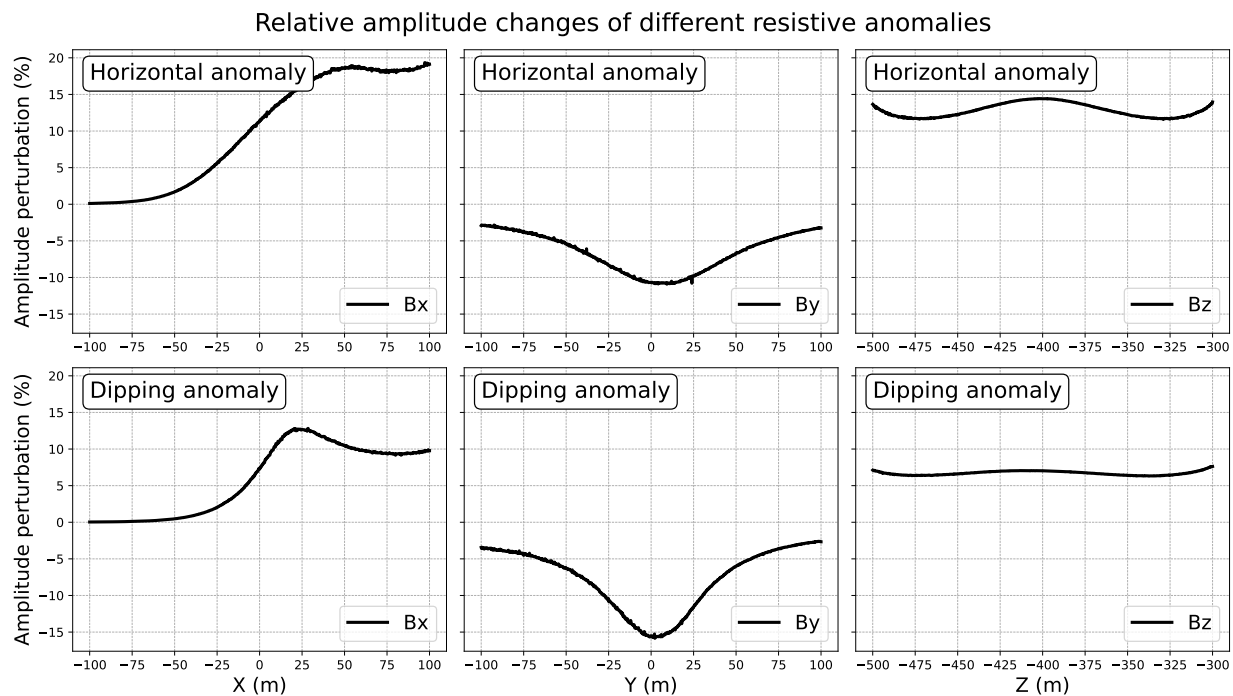

Figure 10. Relative amplitude changes along three magnetic sensing fibers due to horizontal (first row) and dipping (second row) electrical resistivity anomalies.

4   FIRST FIELD TRIAL

In March 2023 we carried out the first small-scale field trial of the distributed magnetic sensing system at the Center for Photonics Technology facility in Blacksburg, VA. Here, we describe the experiment design as well as providing an initial look at the data acquired by the distributed magnetic sensing fiber.

4.1   Design of Experiments

We perform an active source field experiment using a bass shaker and solenoid as seismic and electromagnetic sources, respectively, to evaluate the sensitivity of the proposed multi-physics optic fiber. The fiber comprises a single-mode core and two Metglas wires in the fused silica cladding, with an estimated optimal core distance and azimuth. To enhance the signal-to-noise ratio and be compatible with Sentek Instrument's DASnova interrogator, fiber Bragg grating with $2\,m$ channel/gauge spacing is employed. The multi-physics fiber's length is $10\,m$, and we place a conventional single-mode optic fiber of the same length next to it, connected by a splicer and buried with sand. The conventional fiber is sensitive to acoustic motions only and serves as a reference to verify the absolute amplitude and test the acoustic and magnetic strain's separation accuracy recorded by the multi-physics fiber. We also deploy additional geophones in the same trench to compare the recorded strain with the indirect gradient formulation. The acquisition geometry is shown in Figure 11.

This report primarily focuses on the analysis of recordings obtained from the controlled electromagnetic source. Initially, the solenoid is positioned above the buried fibers and then gradually moved away from the trench. A fixed-strength alternating sinusoidal current is applied to the solenoid, exciting a series of frequencies one by one.

4.2   Initial Views of Data

In the data, we observe sensitivities to the time frame of observation, H_0, and f_s similar to the model prediction. However, the model and data do not agree perfectly for a few reasons: there is no iron bar included in the model (whereas there is one in the solenoid in the experiment), the model assumes a single domain when there are many in reality, the source is not a perfect sinusoidal function in the experiment, there is material between the solenoid and the fiber, and there is noise from a few sources at the experiment site.
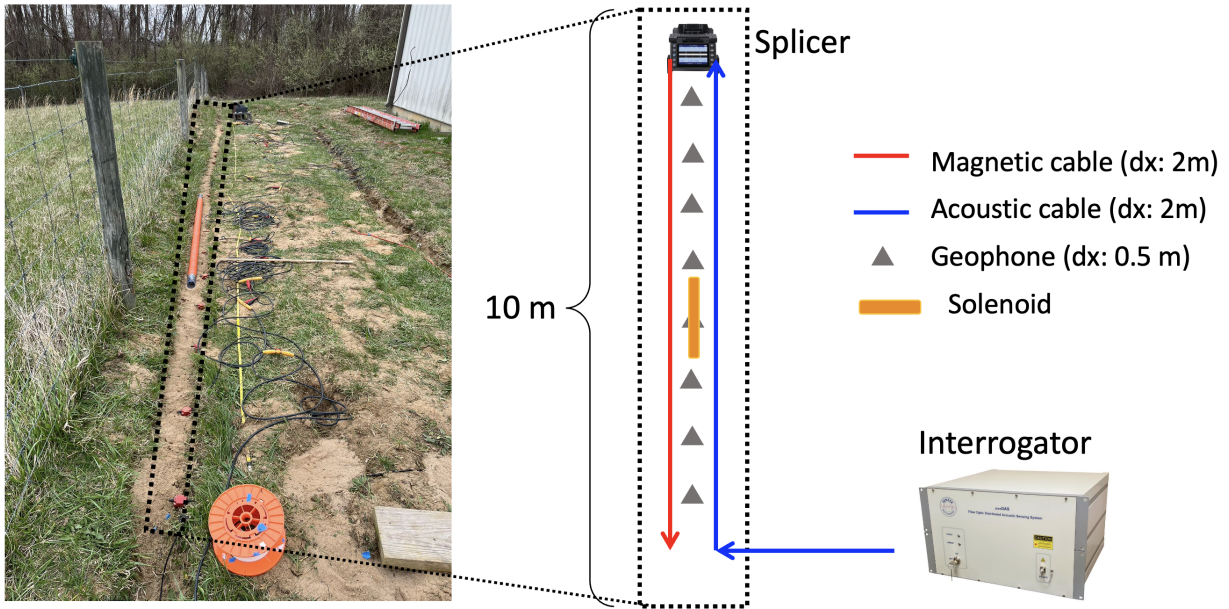
Figure 11. Field experiment layout.

The model predicts different results based on the time of observation, Figure 6 which is seen in the experiment as well. Figure 12 shows two amplitude spectra recorded for a 50 Hz source on top of the fiber with starting times for the first recording at $t = 0$ and the second recording at $t \approx 10 \ s$. Both recordings are five seconds long. The amplitude spectrum for the recording starting from $10 \ s$ contains less harmonics and lower amplitudes for all response frequencies and different relative harmonic amplitudes. The model predicts an effect like this for different time frames as shown for 50 Hz in Figure 12. While the model does not predict the response amplitudes of the experiment for reasons discussed previously, it does predict a change in relative amplitudes based on the time frame of observation. One possible explanation of the differences in harmonic amplitude distribution over time in the actual fiber that is the fact that the state of polarization of the light source changes over time and therefore the light "sees" different strain components in the fiber. If this explanation is correct, we would expect time-dependent effects to disappear in the nano-wire fiber where the nano-wires are uniformly distributed around the fiber azimuth (assuming perfect drawing). If the drawing is not perfect, we may see time-dependent effects as seen in the data. Eliminating the polarization dependence either by changing the fiber or interrogation would eliminate effects related to polarization dependence which should not exhibit significant non-linearity - effects from the LLG non-linearity would still be present. Adjustments to the model can be made to create a model that better predicts the response amplitudes based on the field experiment conditions.

In the field, we observed the experimental sensitivity to changes in H_0 by moving the solenoid further from the fiber optic cable. Since the magnetic field decays with distance from the solenoid, moving the solenoid further from the fiber is similar to decreasing H_0 in the model. Figure 13 shows an example of the data at $f_s = 100$ Hz on top of the fiber and $0.5 \ m$ away from the fiber. In this data, we see a significant decrease in amplitude of the signal from on top of the fiber to $0.5 \ m$ away from the fiber. The peaks at 100 Hz and 200 Hz are visible in the data, but the harmonics are not apparent $0.5 \ m$ away. This decrease in amplitude increases the further away from the fiber the solenoid is and at $1 \ m$ away (not shown) the magnetostriction signal is not visible in the data. Model comparisons are also shown in Figure 13 for a source at $f_s = 100$ Hz and $H_0 = 0.5 \ kA/m$ and $H_0 = 0.01 \ kA/m$. The model source amplitudes are not the same amplitudes as measured in the field; however, these two images also demonstrate a significant decrease in response amplitude.

The response amplitude sensitivity to f_s is also observable in the field data. Figure 14 shows how the response amplitude decreases drastically from a source with frequency of 1250 Hz to 1500 Hz and amplitude $H_0 = 1 \ kA/m$. The model also predicts a drastic decrease in the response amplitude; however, what is very interesting about this case is that the model predicts period doubling at 1500 Hz, but not 1250 Hz. Period doubling is a characteristic typical of non-linear systems (Taylor, 2005), which means there might be a certain threshold source frequency where the period doubling occurs, causing a decrease in the response amplitude at the source frequency with period doubling present. The period doubling is not visible in the data which could be due to the background noise. However, there is a subharmonic visible in the data at 500 Hz that may be due to LLG non-linearity. The
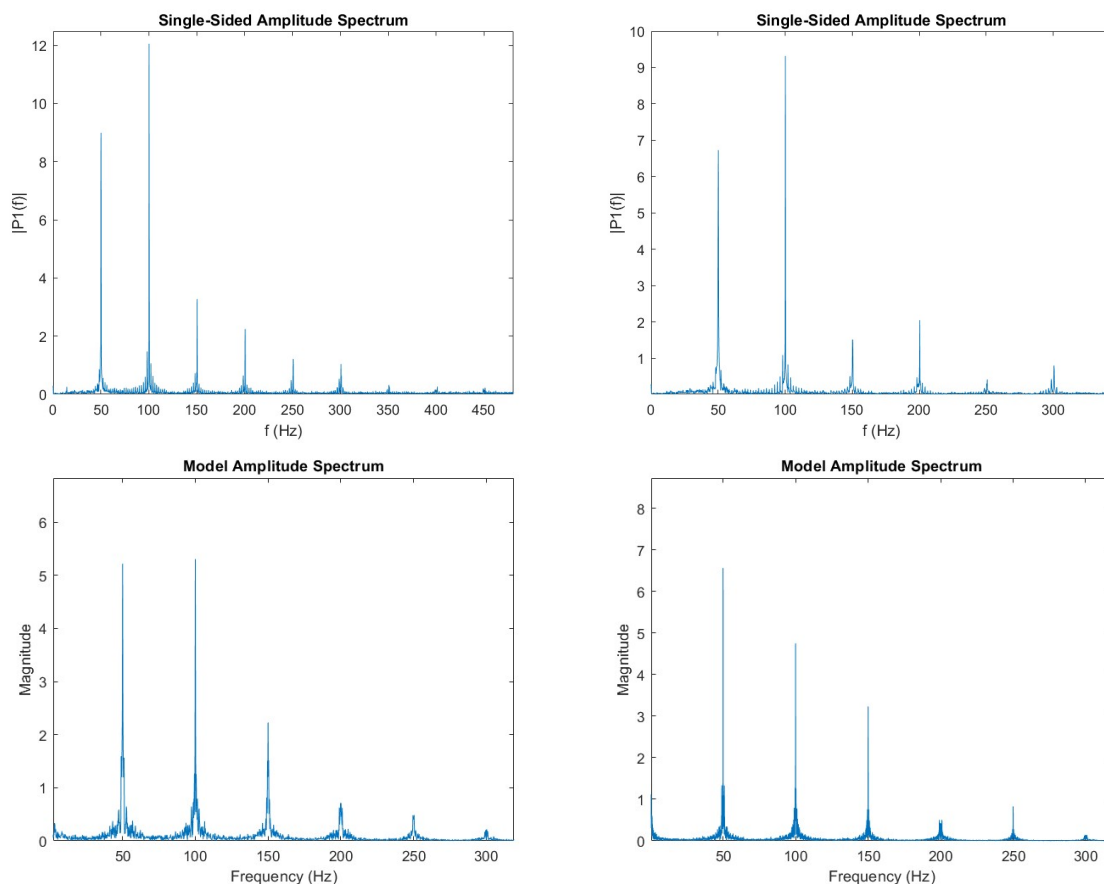
Figure 12. Examples of data at channel 30 for a source frequency of 50 Hz with the solenoid on top of the fiber (top). The data shown was recorded for the first (left) and third shot (right), which started recording about five seconds after the recording of the first shot ended. The the model prediction for a 50 Hz source (bottom) from $0\ s$ to $5\ s$ (left) and $10\ s$ to $15\ s$ (right).

subharmonic being generated by the current amplifier or the interaction between the amplifier and the inductance of the coil is one other possible cause which can be confirmed by analyzing the voltage waveform over the coil by an oscilloscope. It may be useful to set up experiments in the lab to observe and confirm that this phenomenon occurs in the real system and not just the model. The order of magnitude drop in the fiber signal and the existence of the subharmonic does however provide some evidence that the system in the field exhibited this non-linear characteristic since we observe this large drop in magnitude in the model predictions as well.

5   DISCUSSION AND CONCLUSIONS

Through magnetostrictive modeling, we were able to confirm the observed spectral response of strain caused by an external magnetic field during a field experiment. By examining the changes in the relative amplitude of various harmonics based on the strength of the source and the initial angle of the magnetization vector, we gained insight into how we can enhance the magnetic sensitivity of the fiber.

One of the most important pieces of information gathered from the field data is that the multi-physics optic fiber is sensitive to the solenoid source to only about $0.5\ m$ away. Clearly future experiment designs should be improved to increase the fiber sensitivity and to incorporate use of a stronger magnetic source since the distances will be much larger for actual surveys. The minimum magnetic flux density that the tested fiber can detect is still much higher than that of state-of-the-art EM magnetometers, at roughly a few microtesla. One way of improving sensitivity is magnetic annealing (Cullity and Graham, 2009). Recent lab experiments have demonstrated that the sensitivity of magnetic sensing fibers can be improved through magnetic annealing, with
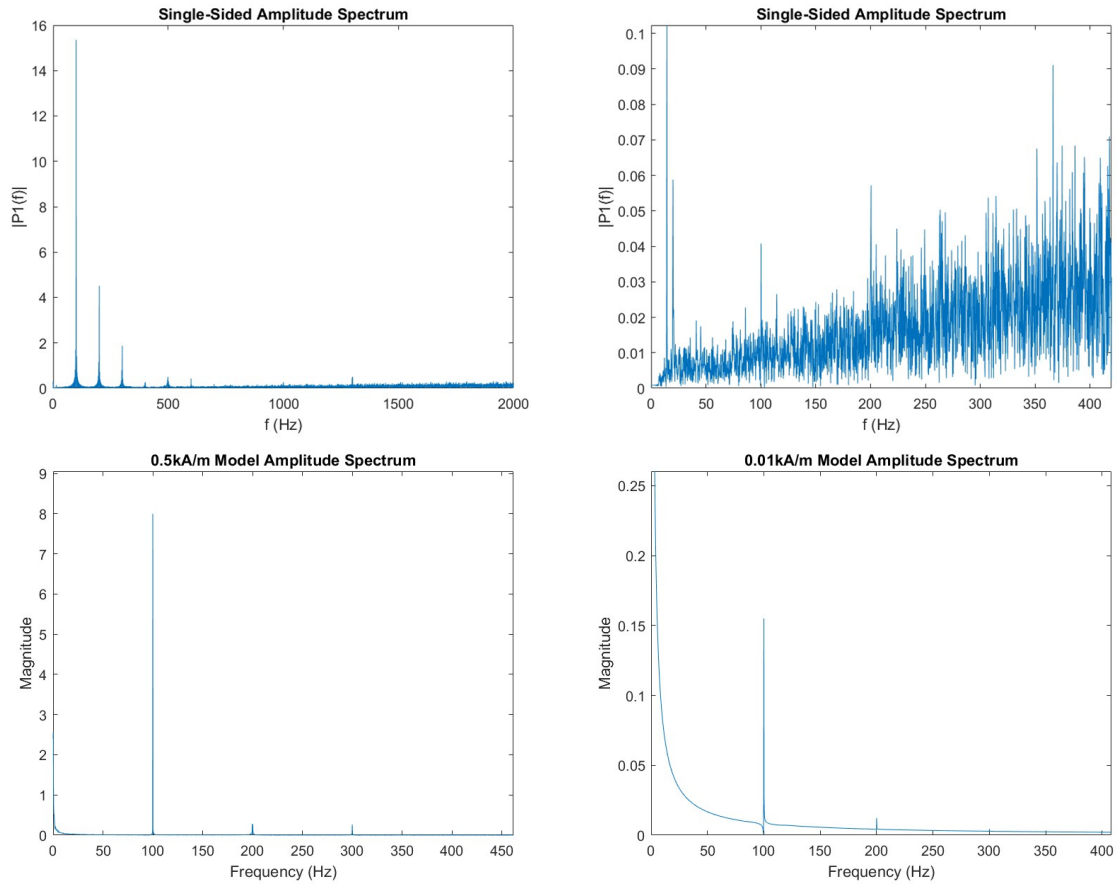
Figure 13. Examples of the data for a source frequency of 100 Hz (top). The data shown was taken when the solenoid was on top of the fiber (top left) and 0.5 m away from the fiber (top right). The model responses are also shown for $H_0 = 0.5 \ kA/m$ (bottom left) and $H_0 = 0.01 \ kA/m$ (bottom right). The model predicts the decrease in response amplitude seen in the data.

a potential lower limit of approximately 10-100 nanotesla achievable during the draw tower process with the application of an external static magnetic field. Additionally, the sensitivity can be further optimized by adjusting the number, spacing, and size of the Metglas cladding. Fiber optic sensing also provides orders of magnitude higher spatial sampling than conventional point sensors, with continuous measurement capabilities that allow for improved signal-to-noise ratios through spatial averaging. These options and others will be explored in more detail in the future to determine how effective each method is.

This report primarily focuses on the magnetic component of sensing cables. However, in practical applications, the direct output of strain or strain rate from the interrogator results from both magnetic and acoustic wavefields. Therefore, it may be necessary to properly separate these two strains if we want to conduct conventional seismic and electromagnetic inversion to infer subsurface structure. While ignoring the influence of ambient seismic and electromagnetic noise levels, the magnetic-related strain and seismic-related strain can overlap in the time, frequency, and time-frequency domains. Separating them in the first two scenarios may be straightforward, but in cases where they overlap in both time and frequency domains, it may be necessary to use blind source separation techniques, such as independent component analysis, to distinguish the magnetic response from the seismic one (Morgan, 2022).

In a conventional cross-well CSEM survey, data is collected by positioning the receivers at depth in one well and moving a powerful EM transmitter continuously through another well. The receiver string is moved to the next position after the transmitter has passed over the entire interval, and the process is repeated until data have been collected at multiple receiver stations. The number of receiver stations in a typical survey can range from 32 to 60, and the survey generally takes between 16 and 36 hours to complete (DePavia et al., 2008). The proposed distributed magnetic sensing system can significantly reduce the time and effort required for cross-well CSEM surveys by simplifying the source-receiver loop to a single-level source loop.

The distributed magnetic sensing system also shares several operation benefits similar to those of optical fiber sensing methods,
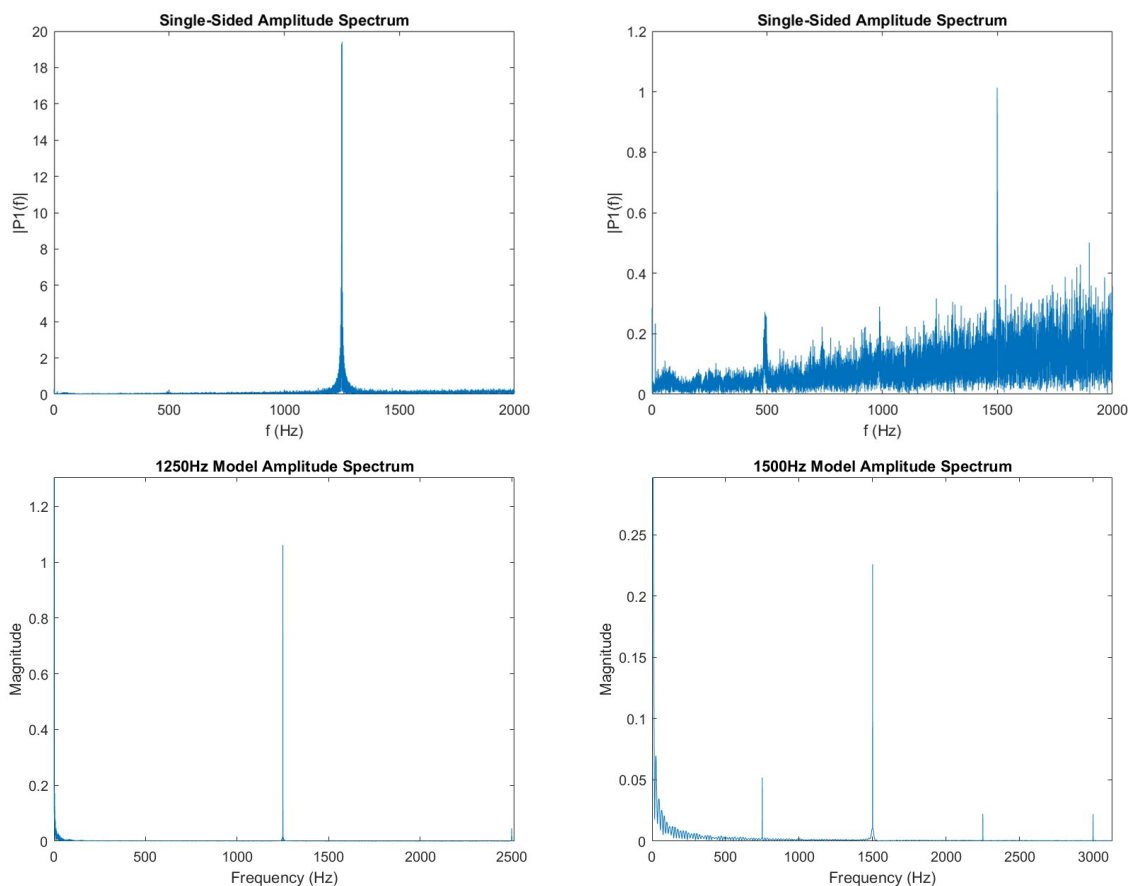
Figure 14. The data for source frequencies of 1250 Hz (top left) and 1500 Hz (top right) with the solenoid on top of the fiber. The model responses to 1250 Hz (bottom left) and 1500 Hz (bottom right) predict the decrease in response amplitude seen in the data. Interestingly, the 1500 Hz model response exhibits period doubling.

such as real-time monitoring, durability, and reduced cost. Additionally, it can be deployed more easily than conventional sensors, allowing for wider spatial coverage of the target area. The increased azimuth and spatial sensitivity can provide better constraints of the structural changes and reduce uncertainties during time-lapse CSEM inversions.

6   ACKNOWLEDGEMENTS

REFERENCES

Cullity, B., and C. Graham, 2009, Introduction to magnetic materials, 2 ed.: John Wiley & Sons, Inc.

DePavia, L., P. Zhang, D. Alumbaugh, C. Leveque, H. Zhang, and R. Rosthal, 2008, Next-generation crosswell em imaging tool: Presented at the SPE Annual Technical Conference and Exhibition, OnePetro.

Dormand, J., and P. Prince, 1980, A family of embedded runge-kutta formulae: Journal of Computational and Applied Mathematics, **6**, 19–26.

Gilbert, T. L., 2004, A phenomenological theory of damping in ferromagnetic materials: IEEE Transactions on Magnetics, **40**, 3443–3449.

Hileman, Z., D. Homa, L. Ma, B. Dong, E. Martin, G. Pickrell, and A. Wang, 2022, Development of a multimaterial optical fiber for fully distributed magnetic sensing applications: IEEE Sensors Letters, **6**, 1–4.

Lakshmanan, M., 2011, The fascinating world of the landau–lifshitz–gilbert equation: an overview: Philosophical Transactions of the Royal Society A: Mathematical, Physical and Engineering Sciences, **369**, 1280–1300.

Morgan, S. E., 2022, Improving separation of signals from multiple physical quantities detected by sensor arrays: Master's thesis, Virginia Tech.

Rochlitz, R., N. Skibbe, and T. Günther, 2019, custem: Customizable finite-element simulation of complex controlled-source electromagnetic data: Geophysics, **84**, F17–F33.

Shoemaker, K., 2018, The mathematical modeling of magnetostriction: Master's thesis, Bowling Green, OH.

Smith, R. K., M. Grabowski, and R. Camley, 2010, Period doubling toward chaos in a driven magnetic macrospin: Journal of Magnetism and Magnetic Materials, **322**, 2127–2134.

Taylor, J. R., 2005, Classical mechanics: University Science Books.

Wieser, R., 2015, Description of a dissipative quantum spin dynamics with a landau-lifshitz/gilbert like damping and complete derivation of the classical landau-lifshitz equation: The European Physical Journal B, **88**.